JOURNAL OF AIRCRAFT
Vol. 46, No. 1, January–February 2009

High-Altitude Limit Cycle Flutter of Transonic Wings

Oddvar O. Bendiksen*
University of California, Los Angeles, Los Angeles, California 90095-1597

DOI: 10.2514/1.36413

In flutter testing, it is often implicitly assumed that the most critical case at any given Mach number will occur at sea level conditions. This is a reasonable expectation, as the highest dynamic pressure at a fixed Mach number will be encountered at sea level, where the air density is highest. In the present paper, a counterexample involving a generic swept wing representative of transport aircraft is presented in which transonic limit cycle flutter is predicted to occur at altitude rather than at sea level. The calculations are based on a time-accurate Eulerian–Lagrangian finite element scheme that fully accounts for both structural and aerodynamic nonlinearities arising from large deflections and shock motion. Flutter onset is around Mach 0.84 and the limit cycle amplitudes grow until Mach 0.95 is reached, at which point they start decreasing, vanishing abruptly around Mach 0.97. The limit cycle flutter persists down to very low air densities, corresponding to altitudes above 75,000 ft, and the maximum limit-cycle-oscillation flutter amplitude does not occur at sea level, but at altitude. If sufficient structural damping is added, the wing will be flutter-free at lower altitudes but not at higher (cruise) altitudes. At Mach 0.95, the wing is stable below about 15,000 ft, even in the absence of structural damping, but experiences strong limit cycle flutter at higher altitudes.

Nomenclature

A	=	aspect ratio
C_p	=	pressure coefficient $[(p - p_\infty)/\frac{1}{2}\rho_\infty U_\infty^2]$
c	=	airfoil or wing chord ($2b$)
E	=	Young's modulus
E_{tot}	=	total energy of wing ($T + U$)
G	=	shear modulus
k	=	reduced frequency ($\omega b/U_\infty$)
M	=	Mach number
m	=	mass per unit span
p	=	pressure
T	=	kinetic energy
t	=	time
U	=	strain energy
$\boldsymbol{U}$	=	mesh velocity vector with components U_i
U_∞	=	freestream velocity at upstream infinity
u, v, w	=	plate or wing displacements in the x, y, z directions
$\boldsymbol{u}$	=	fluid velocity vector with components u_i
α	=	angle of attack
β_x, β_y	=	rotations of normals in the x–z and y–z planes
γ	=	ratio of specific heats
Λ	=	sweep angle
λ	=	taper ratio
ρ	=	density
τ	=	nondimensional time ($\omega_{1T} t/2\pi$)
ω	=	circular frequency
ω_{1T}	=	frequency of first torsion mode in vacuum

Subscripts

LE, TE	=	leading and trailing edges
∞	=	conditions at upstream infinity

I. Introduction

IN THE strictly subsonic region, in which the freestream Mach number M_∞ is less than the critical Mach number M_{cr} required to produce locally sonic flow, slender wings are susceptible to bending-torsion flutter. This aeroelastic instability is especially dangerous, because energy is extracted from the airstream at a sufficient rate to produce rapidly increasing flutter amplitudes. In the transonic region, on the other hand, the presence of shocks on the wing surface introduces strong aerodynamic nonlinearities and limit cycle flutter† becomes the rule rather than the exception [1–3]. Structural nonlinearities [4] can also result in LCO-type flutter at subsonic as well as supersonic Mach numbers, but the nature of the transonic flutter instability is usually very different.

Transonic limit cycle flutter can occur even in the absence of structural nonlinearities, as the shock motion transitions from Tijdeman type A (continuous) to type B (intermittent), which results in a rapid decrease of the aerodynamic work done on the wing [5]. The resulting flutter mode typically has bending and torsion almost perfectly in phase at each span location, and the 2-D streamwise wing-section motion resembles a single-degree-of-freedom (SDOF) torsion mode with an axis of rotation forward of the leading edge. Intermittent trailing-edge separation has a similar effect and, in many cases, triggers transition to type B shock motion at an earlier stage than would occur in a fully attached flow. But the existence of small-amplitude LCOs, as observed in a number of wind-tunnel tests [6,7], suggests that mechanisms other than flow separation or structural nonlinearities can also cause LCO-type flutter.

The transonic limit cycle flutter observed during wind-tunnel tests [8] at DLR, German Aerospace Center, in Göttingen of a high-aspect-ratio swept wing representative of a transport aircraft provides an interesting challenge from a theoretical standpoint. First, because the LCO-type flutter was encountered at an angle of attack and lift coefficient close to typical cruise conditions, it cannot be classified as stall flutter, nor is it evident from the experimental data that trailing-edge separation played a role. Second, because the LCO was observed on a clean wing, the effects of stores or wing-mounted engines can also be ruled out.

In [9], we concluded that the aeroelastic mechanism responsible for the LCO-type flutter of the Göttingen wing appears to be fundamentally different from the mechanisms responsible for LCO flutter of low-aspect-ratio wings typical of fighter aircraft. In the case of the high-aspect-ratio swept wing, the structural washout effect from aeroelastic deformations plays a fundamental role in throttling the energy flow from the airstream to the wing, resulting in limit cycle

Presented as Paper 2017 at the 48th AIAA/ASME/ASCE/AHS/ASC Structures, Structural Dynamics, and Materials Conference, Honolulu, HI, 23–26 April 2007; received 31 December 2007; revision received 8 September 2008; accepted for publication 9 September 2008.

*Professor, Department of Mechanical and Aerospace Engineering. Associate Fellow AIAA.

†Also referred to as limit cycle oscillations (LCO) in this context.

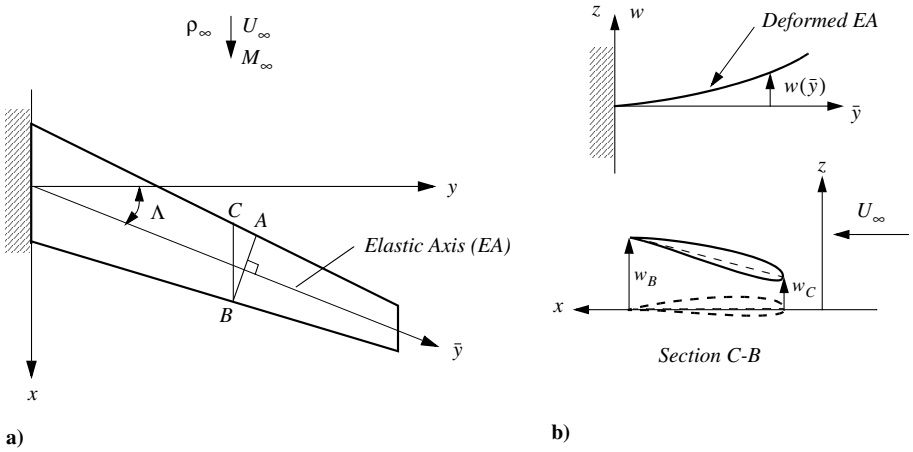

Fig. 1 Elastic deformations of a swept wing: a) chordwise segment *A-B* vs streamwise segment *C-B* and b) structural washout effect (reduction of angle of attack of streamwise segment *C-B* because $w_C < w_B$).

flutter. The structural washout effect is illustrated in Fig. 1 and arises from the fact that streamwise and chordwise segments undergo different rotations about the unswept *y* axis. As the wing bends, the washout reduces the angle of attack of streamwise chord sections, unloading the outboard region of the wing, reducing the shock strength, and shifting the part-chord shocks in the upstream direction. The weaker and more forward shocks lead to an earlier transition (at lower amplitudes) from type A to type B shock motion, resulting in a limit cycle flutter mode that persists over a relatively wide range of dynamic pressures and air densities (altitudes). Based on calculations on a generic transport wing (the G-wing), it was concluded that the LCO-type transonic flutter observed on the Göttingen wing should also be expected in the case of other swept wings of high aspect ratio and similar flexibility.

The present paper addresses three surprising results obtained in the previous study [9] that remain to be explained. First, it was found that a nonlinear structural model was needed to capture the observed LCO behavior of these wings. When a linear structural model was used, the critical dynamic pressure at LCO onset was overestimated by a factor of nearly 3, and the predicted flutter mode was at a frequency much higher than was observed in the wind tunnel. Second, it was found that transonic LCO-type flutter persists down to very low dynamic pressures if the flight Mach number is held constant. Third, for wings of representative flexibility, the aeroelastic washout effect can lead to the counterintuitive result that increasing the dynamic pressure may actually be stabilizing, causing a decrease in the LCO amplitudes. In such a case, *decreasing* the dynamic pressure may *increase* the LCO amplitude (see Fig. 2). This would suggest that transonic flutter at high altitudes may become possible, even if the wing is stable at lower flight altitudes. It is also of relevance in wind-tunnel testing, in which bypass or blowout valves are often used to rapidly drop the tunnel dynamic pressure (or density) when flutter onset is encountered.

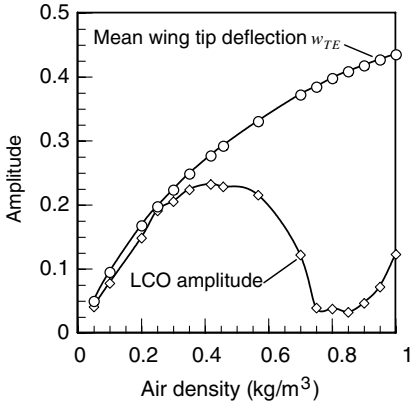

Fig. 2 LCO amplitude and mean wing tip deflection at trailing edge vs air density for the G-wing studied in [9]. In this and all subsequent figures, wing displacements are normalized with respect to wing root chord. Note the LCO amplitude reversal around $\rho = 0.4$ kg/m^3; $M_\infty = 0.865$.

The paper has two primary objectives. The first objective is to identify the mechanism responsible for the anomalous LCO flutter behavior vs air density predicted for the G-wing and to examine under what conditions high-altitude flutter might become possible and at what Mach numbers. The second objective is to provide an explanation for the large difference between the transonic stability predictions of the linear structural model, as compared with the nonlinear model: in particular, why the stiffer nonlinear model predicts a less stable wing and significantly *larger* LCO amplitudes.

The results presented in this paper demonstrate that the LCO-type flutter of the G-wing is a *transonic* phenomenon. No limit cycle flutter was observed at subcritical Mach numbers, and the LCO abruptly vanished at around Mach 0.97. At Mach 0.865, there are indications that multiple (nested) LCOs may be present, and the limit cycle amplitude depends on the initial conditions. The results indicate that the maximum LCO flutter amplitude for this class of wings does not occur at sea level or low altitudes, but closer to typical cruising altitudes. For example, in the case of the G-wing at Mach 0.865, the LCO amplitude peaks at around a density altitude of 33,000 ft. If sufficient structural damping is added, the wing will be flutter-free at the lower altitudes, but not at higher altitudes. At higher transonic Mach numbers, at or close to Mach 0.95, the flutter amplitudes continue to grow with altitude well into the stratosphere, to 75,000 ft and beyond, yet the wing is stable below about 15,000 ft. To the author's knowledge, there have not been any definite experimental or theoretical studies of this phenomenon, referred to in this paper as *high-altitude flutter*, although he is aware of anecdotal evidence of encounters with the phenomenon during flight tests.

II. Computational Approach

The calculations are based on a nonlinear time-accurate finite element formulation, applicable to a general class of aeroelastic problems with large deformations. The formulation makes use of individual element-fixed local Lagrangian coordinate systems in addition to a global Eulerian system, as shown in Fig. 3. Calculations are done at the finite element level, both in the fluid and structural domains, and the fluid–structure system is time-marched as a single dynamical system using a multistage Runge–Kutta scheme. The exact nonlinear boundary condition at the wing surface is satisfied using the actual deformation of the wing, as defined by the finite element shape functions and the local element coordinates, and the generalized aerodynamic forces associated with the in-plane and out-of-plane degrees of freedom are calculated in the local Lagrangian (element) coordinate systems that fully account for large rigid-body translations and rotations. Further details can be found in [9,10].

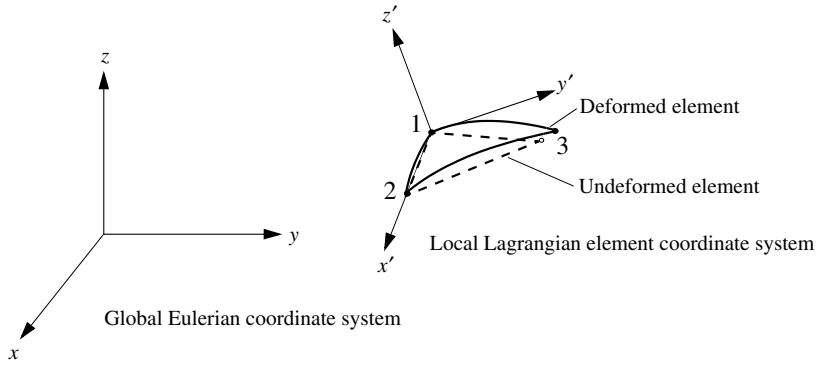

Fig. 3 Eulerian and Lagrangian coordinate systems used in the direct Eulerian–Lagrangian computational scheme.

A. Nonlinear Structural Model

Figure 3 shows a typical triangular structural finite element in its deformed configuration. The xyz coordinate system is a fixed Eulerian reference frame with respect to which the response of the wing structure is expressed, and the $x'y'z'$ system is an element-fixed local coordinate system that moves with the corresponding element at all times. It is Lagrangian in the sense that the axes are fixed to three points in the structural element. The elastic deformations of each element are expressed relative to these local systems.

At any given step in the time-marching solution, the three corner nodes of the triangular finite element form a plane. The z' axis is defined orthogonal to this plane by taking the cross product of the two planar vectors from the origin (node 1) to the remaining two nodes. The x' axis is aligned along nodes 1 and 2 of the triangular elements, and the y' axis orientation is determined so that a right-handed coordinate system is formed. Displacements and forces can then be expressed in either the local element coordinates or the global system coordinates, and the two representations are related through an orthogonal transformation involving the direction cosines between the axes.

The nonlinear structural model employs three basic finite elements to model the in-plane, out-of-plane, and nonlinear behaviors, as shown in Fig. 4. A Mindlin–Reissner discrete shear triangle (DST) is used to model the out-of-plane bending and the transverse shear behavior. This element is based on the formulation in [11] and extended to dynamics problems. It is free of shear locking and converges to the discrete Kirchhoff triangular elements when the shear deformations become negligible.

A constant strain triangle (CST) models the in-plane behavior, and its shape functions are used together with the corresponding shape functions of the DST element to create the stress-stiffening matrix in local element coordinates. The stress-stiffening matrix provides the nonlinear coupling between in-plane and out-of plane displacements. It is based on the von Kármán plate theory, which assumes that the nonlinear strain components arising from the in-plane displacement gradients are small compared with the corresponding terms arising from the transverse displacement gradients and may therefore be neglected. This is a reasonable assumption in the present calculations, because the deformations relative to the local Lagrangian element coordinate systems are always small if linearly elastic behavior of the wing is assumed.

The total strain energy of an element can be expressed as

$$U^e_{\text{total}} = U_m + U_b + U_s + U_{N1} + U_{N2} \tag{1}$$

where U_m, U_b, and U_s are the quadratic-order strain energies representing the membrane stretching (CST), out-of-plane bending, and shear (DST), respectively. The cubic-order strain energy U_{N1} represents the nonlinear coupling of the in-plane and out-of-plane motion, and the quartic-order strain energy U_{N2} represents the nonlinear coupling effect of slope due to large deflections. To obtain an element free of shear locking, the equilibrium equations are used to solve for the transverse shear strains, with the help of the constitutive equations. The stiffness matrix is then formulated using quadratic interpolation functions for the rotation fields. The stiffness matrix for the in-plane CST element is based on linear interpolation functions.

The element stiffness matrix of the nonlinear model can be obtained from the principle of stationary potential energy, using the strain energy relations, and is of the form

$$\begin{aligned} [K_e]_{15\times 15} &= \begin{bmatrix} [\text{DST}] & [\text{NLC}] \\ [\text{NLC}]^T & [\text{CST}] \end{bmatrix} \\ [\text{DST}]_{9\times 9} &= \text{out-of-plane partition} \\ [\text{CST}]_{6\times 6} &= \text{in-plane partition} \\ [\text{NLC}]_{9\times 6} &= \text{nonlinear coupling partition} \end{aligned} \tag{2}$$

To calculate the nonlinear coupling partition, the values of the nodal degrees of freedom are required at the current time step. The deformed unit vectors are updated at each time step by the incremental rotations in the global x and y directions, using finite

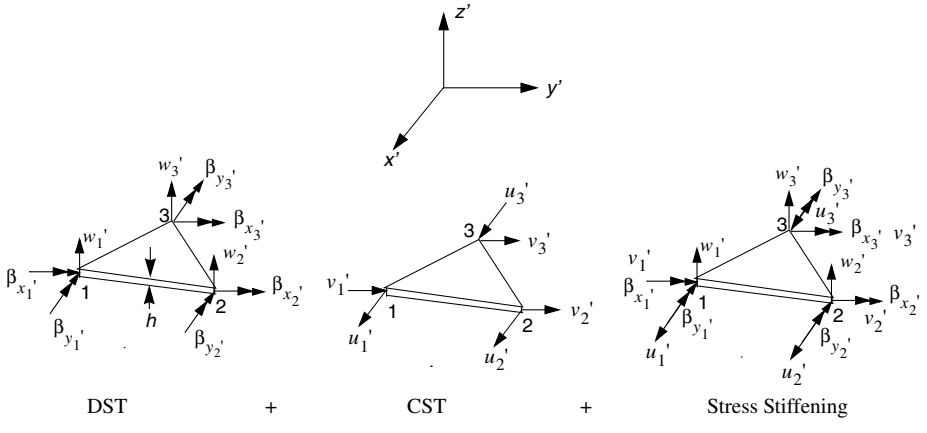

Fig. 4 Components of the nonlinear Mindlin–Reissner plate finite element.

rotation relations. Cubic interpolation functions are used as a basis for deriving the consistent mass matrix and the generalized aerodynamic loads. All integrals are evaluated using Gaussian integration in natural (triangular) coordinates.

B. Nonlinear Aerodynamic Model

The aerodynamic model is based on a Galerkin finite element discretization of the weak or integral form of the conservation laws:

$$\frac{\partial}{\partial t}\int_{\Omega} \boldsymbol{W}\mathrm{d}V + \int_{\partial\Omega} \boldsymbol{F}\cdot\boldsymbol{n}\mathrm{d}S = 0 \tag{3}$$

where Ω is an element volume with boundary $\partial\Omega$ moving with velocity $\boldsymbol{U}$, $\boldsymbol{n} = n_i\boldsymbol{e}_i$ is the outward unit normal to $\partial\Omega$, $\boldsymbol{e}_i$ are the unit vectors in the x_i directions, and

$$\boldsymbol{W} = \begin{bmatrix} \rho \\ \rho u_1 \\ \rho u_2 \\ \rho u_3 \\ \rho e \end{bmatrix} \qquad \boldsymbol{F}_j = \begin{bmatrix} \rho(u_j - U_j) \\ \rho u_1(u_j - U_j) - \sigma_{1j} \\ \rho u_2(u_j - U_j) - \sigma_{2j} \\ \rho u_3(u_j - U_j) - \sigma_{3j} \\ \rho e(u_j - U_j) - \sigma_{ij}u_i \end{bmatrix} \tag{4}$$

where ρ is the density; $\boldsymbol{u}$ is the material velocity; e is the total energy per unit mass; u_j and U_j are the Cartesian components of $\boldsymbol{u}$ and $\boldsymbol{U}$, respectively; σ_{ij} is the Cartesian stress tensor; and $\boldsymbol{F} = \boldsymbol{F}_j\boldsymbol{e}_j$. In the inviscid (Euler) flow model used in this paper, $\sigma_{ij} = -p\delta_{ij}$, and the equation of state can be used to eliminate the pressure p. A typical Galerkin finite element discretization results in a space-discretized set of nodal equations for the fluid domain of the form [12]

$$\frac{d}{dt}\sum_j \boldsymbol{m}_{ij}\boldsymbol{W}_j + \boldsymbol{Q}_i - \boldsymbol{D}_i = 0 \tag{5}$$

where $\boldsymbol{W}_j$ are the nodal values of $\boldsymbol{W}$, and the summation on j extends over all nodes in the superelement or control volume associated with node i (i.e., the union of all elements that meet at node i). Here, $\boldsymbol{m}_{ij}$ is the consistent mass matrix, $\boldsymbol{Q}_i$ is the flux vector, and $\boldsymbol{D}_i$ is a vector of dissipative fluxes of the Jameson–Mavriplis type [13,14], as modified in [15,16].

A finite element discretization of the structural domain (wing structure) leads to a similar set of equations, in terms of suitable generalized Lagrangian displacement coordinates $\boldsymbol{q}_j$:

$$\frac{d}{dt}\sum_j \boldsymbol{m}_{ij}\dot{\boldsymbol{q}}_j + \boldsymbol{Q}_i^E + \boldsymbol{Q}_i^D - \boldsymbol{Q}_i^F = 0 \tag{6}$$

where the sum (assembly) must be carried out over all elements that meet at node i. Here, $\boldsymbol{Q}_i^E$ are the nonlinear elastic forces, $\boldsymbol{Q}_i^D$ are the structural damping forces, and $\boldsymbol{Q}_i^F$ are the consistent generalized fluid forces associated with the ith node.

A multistage Runge–Kutta scheme is used to integrate the space-discretized system of nonlinear equations forward in time. To maintain time accuracy and strict fluid–structure synchronization, the fluid and structural finite element equations are time-marched simultaneously, within the same multistage Runge–Kutta execution loop.

C. Fluid–Structure Coupling

The space-discretized equations for the fluid and structure are coupled through the boundary condition at the fluid–structure boundary, which for the Euler equations is the kinematic boundary condition of tangent flow. To prevent spurious momentum and energy production at the wing-fluid boundary, the numerical implementation of the boundary condition is based on the *actual* state of the physical wing surface, as defined by the finite element solution. In the aeroelastic code, this is accomplished by working directly with the generalized coordinates and associated shape functions for the structural finite elements. Force vectors are first calculated in the local element coordinate systems using 13-point Gaussian quadrature, and then transformed to the global coordinate system as the space-discretized aeroelastic equations are time-marched. The aerodynamic loads are modeled as *follower forces*, resulting in a more accurate prediction of the aeroelastic response. In the corresponding *linear* structural model, the aerodynamic loads do not enter the aeroelastic code as follower forces, because only the pressure load in the direction normal to the undeformed wing plane is taken into account.

III. Results and Discussion

A. G-Wing

This wing is closely similar in planform (see Fig. 5) to the wind-tunnel model studied in [8], except that the two small trailing-edge kinks have been ignored and the airfoil section is different. We chose the 10%-thick ONERA D airfoil rather than the supercritical airfoil of the Göttingen wing for two reasons. First, we wanted to see if the transonic LCO behavior observed in the wind tunnel was a result of the special nature of the particular supercritical airfoil, and thus an isolated case, or representative of a class of high-aspect-ratio wings with similar mass and stiffness properties. Second, we have extensive experience with the ONERA airfoil in previous transonic flutter calculations for several ONERA M6 wing models [12]. The M6 wing has a similar leading-edge sweep (30 deg) but is of a lower aspect ratio (3.8). No LCO-type flutter of the type seen in the Göttingen wing has been observed in our previous aeroelastic

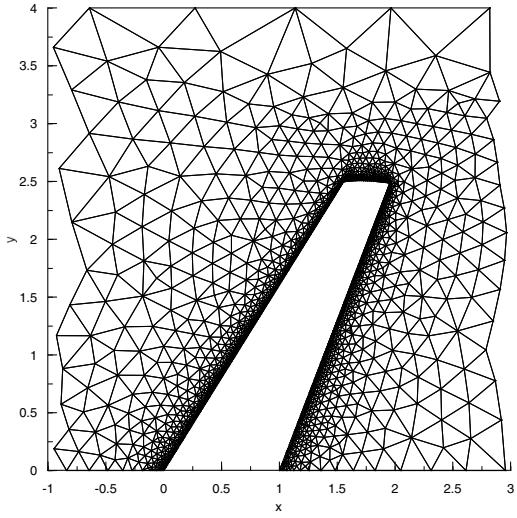

G-Wing

$A = 7.05$
$\Lambda_{LE} = 31.86°$
$\Lambda_{TE} = 21.02°$
$\lambda = 0.41$

Computational Domain
No. of nodes: 43,344
No. of faces: 430,975
No. of cells: 208,926

No. of structural plate elements: 96
No of structural dof's: 168 (linear)
280 (nonlinear)

Fig. 5 G-wing of a planform similar to the wing studied experimentally in [8].

Table 1 G-wing models: frequencies (in hertz) of the first four natural modes

Model	1B	2B	1T	3B
Linear structure	37.82	132.40	272.51	310.10
Nonlinear structure	37.81	133.30	272.63	310.71
Göttingen wing [8]	37.81	112.85	272.60	241.85

calculations involving the M6 wing; however, most of these calculations were carried out using a *linear* structural model.

Using a trial-and-error approach, an attempt was made to match the first few natural frequencies to the experimental frequencies of the Göttingen wing by introducing suitable mass and structural taper along the span. More weights were given to matching the first bending (1B) and first torsion (1T) frequencies, as these would be more important in a flutter analysis. No spanwise mass properties were given in [8], and the stated c.g. of the wing and the mass ratios suggest that the (massive) inboard mounting structure must have been included in the wing weight. For this reason, the mass ratios of the wings could not be matched. The frequencies of the first four modes are shown in Table 1 for both the linear and the nonlinear structural models as well as the Göttingen wing. Contour plots for the first 3 modes are shown in Fig. 6. It should be noted that the third mode of the Göttingen wing is an in-plane mode at a frequency slightly above the second bending mode. Because this mode occurs at a much higher frequency in our G-wing model, it is not included in Table 1.

B. Linear Versus Nonlinear Structure

According to [8], the Göttingen wing entered a stable LCO at Mach 0.865 and a mean lift coefficient in the 0.5–0.6 range. Because of differences in airfoil cambers, this corresponds to an angle of attack of about 4.5 deg for the G-wing with the ONERA airfoil, compared with 2.69 deg for the supercritical Göttingen wing. In addition to trying to match the wing lift coefficient, an attempt was also made to match the mean aeroelastic wing tip deflections, as best they could be estimated from Fig. 16 of [8], to ensure that the structural washout effects were roughly the same in the flutter simulations as in the wind-tunnel tests. In all calculations in this paper, the wing root angle of attack was kept fixed at 4.5 deg.

Calculations based on the linear structural model revealed no LCO-type flutter at and around the air density of $\rho_a = 0.4177$ kg/m^3, corresponding roughly to the wind-tunnel density at which the Göttingen wing exhibited LCO-type flutter if a mass ratio $\mu = 1000$ is assumed.[‡] In fact, the linear G-wing appears stable up through a density of $\rho_a = 1.1$ kg/m^3, but limit cycle flutter does eventually appear at $\rho_a = 1.141$ kg/m^3 (see Fig. 7). However, the frequency of this LCO is significantly higher (94 Hz) than that observed in the wind-tunnel test (50.4 Hz), and the corresponding dynamic pressure is 273% higher than the experimental value. This is in contrast to the calculations using the nonlinear structural model, which reveal limit cycle flutter at the correct air density (see Fig. 8). The LCO flutter mode is essentially the first bending mode of the wing, coupled weakly to the first torsion mode through aeroelastic effects, with each streamwise wing section executing a motion very closely resembling SDOF pitching about an axis upstream of the leading edge. The predicted flutter frequency is 52.4 Hz, which is very close (+4%) to the LCO frequency of 50.4 Hz observed in the wind-tunnel tests.

The reason for the large differences between the LCO amplitudes predicted using the linear vs the nonlinear Mindlin–Reissner finite element model can be understood in terms of the effect that the washout phenomenon has on the transonic flowfield around the wing, especially on the location and motion of the part-chord shocks on the upper wing surface. Although the nonlinear structure is stiffer than the corresponding linear structure, it is actually less stable for this class of wings, because the structural washout is also less. The aeroelastic problem is inherently nonlinear and neither the aerodynamic nor the structural nonlinearities can be ignored, or an incorrect assessment of aeroelastic stability is the likely result.

Two additional features incorporated into the nonlinear structural model could also have a destabilizing effect: 1) the more accurate implementation of the fluid–structure boundary condition, resulting in the generalized aerodynamic loads now entering the problem as follower forces, and 2) the addition of the in-plane degrees of freedom (lead-lag u and foreshortening v) of the wing.

Although it is believed that both would be destabilizing for transonic wings of the G-wing category, additional calculations would be necessary to quantify these effects. In the linear structural model, these forces do not enter the aeroelastic problem as follower forces, because the in-plane degrees of freedom of the wing are not modeled.

C. LCO Amplitude Versus Mach Number

To verify that the predicted limit cycle flutter of the G-wing is essentially a transonic phenomenon, an extensive series of calculations were carried out in the Mach number range from 0.75 through 0.99. No instances of LCO-type flutter were detected at subcritical Mach numbers. Figures 9 and 10 show two typical sets of results for Mach 0.75 and 0.83, respectively. Although the flow around the wing is entirely subsonic (i.e., subcritical) at Mach 0.75 and zero angle of attack, it is slightly past critical when the angle of attack is increased to 4.5 deg. In the latter case, a shock is present near the leading edge, from about 5% of span to the wing tip, with supersonic flow over the forward 10–15% of chord. Because of the far-forward position of the shock, the shock is stabilizing and the dynamic response shows exponential decay (Fig. 9). At Mach 0.83, the shock is slightly forward of midchord, and the decay is very slow because of the closeness to the flutter boundary. Results of calculations at select Mach numbers in the range of 0.84–0.965 are presented in Figs. 11–18 and show that LCO-type flutter persists throughout this Mach number range. Note that at about Mach 0.89, the flutter amplitude starts growing with time, reaching a peak growth rate at around Mach 0.95. Between Mach 0.965 and 0.97, the LCO amplitudes undergo a rapid decay to zero (Fig. 19). At Mach 0.99, at limit cycle of very small amplitude reappears (Fig. 20).

Figure 21 shows the predicted LCO flutter amplitude vs Mach number for an air density of $\rho_a = 0.4177$ kg/m^3, which corresponds to a density altitude of roughly 10 km (32,800 ft). Except in the Mach number range of 0.89–0.96, the LCO amplitudes are stable, although subtle nonclassical behaviors are observed; that is, the motion does not appear exactly periodic, nor does it appear to converge to such a state even after many oscillation cycles. Rather, the flutter mode is better described as *almost periodic* in the sense of Bohr's theory of almost periodic functions [17]. This is reflected in the phase plots as a smearing or broadening of the limit cycle, which is believed to be caused by irreversible (nonconservative) interactions between the structural nonlinearities arising from large deflections and aerodynamic nonlinearities caused by moving shocks on the wing surface. In the Mach number range of 0.89 through 0.95, the limit cycle flutter mode exhibits an amplitude instability, reflected by a slowly growing LCO amplitude at Mach 0.89 (Fig. 14) with a progressively increasing growth rate as the Mach number is increased (Figs. 15 and 16). This instability is believed to be triggered by a weak nonuniformity on the time scale, which causes the basin of attraction of the limit cycle to change with time. Interestingly, the limit cycle is still attracting on a global scale. That is, if the wing is started with a large initial condition, the initial response is a decay to the LCO flutter mode; conversely, a small initial condition results in a rapid amplitude increase to essentially the same initial LCO mode. This behavior is another reminder that we are dealing with an

[‡]The mass ratio or the air density at the LCO flutter point was not stated in [8] and may not be relevant in view of the uncertainty about the inclusion of the mounting structure in the wing weight, as discussed in Sec. III.A. Note that the LCO amplitude is relatively insensitive to air density in the range of 0.35–0.58 kg/m^3 (Fig. 2), corresponding to mass ratios in the range of 720–1200. In the calculations, the proper density scaling was obtained by matching the mean wing tip deflections from Fig. 16 of [8].

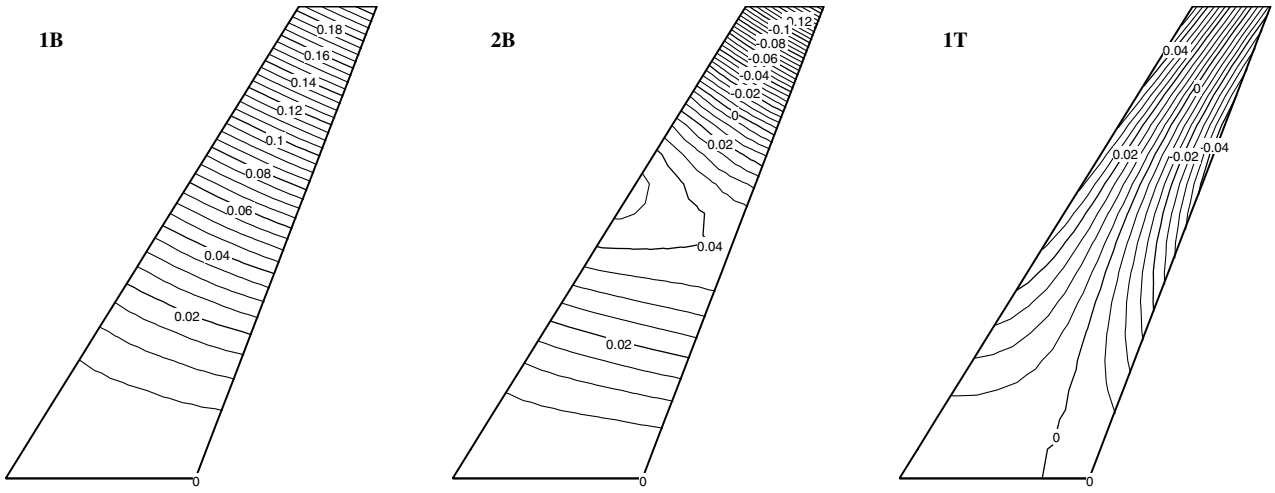

Fig. 6 Contour plots of the first three mode shapes.

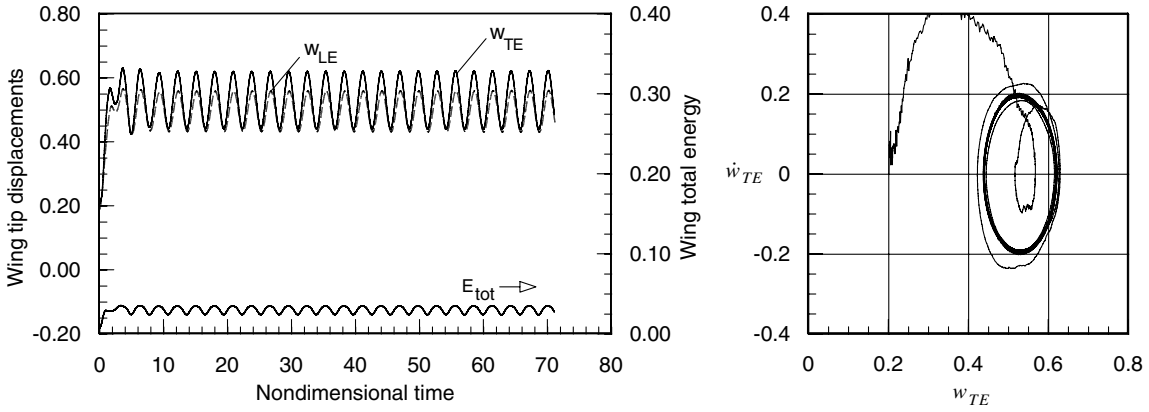

Fig. 7 Limit cycle flutter of the G-wing, as calculated using a linear structural model; $\rho_a = 1.141\ \mathrm{kg/m^3}$; LCO frequency is 90 Hz.

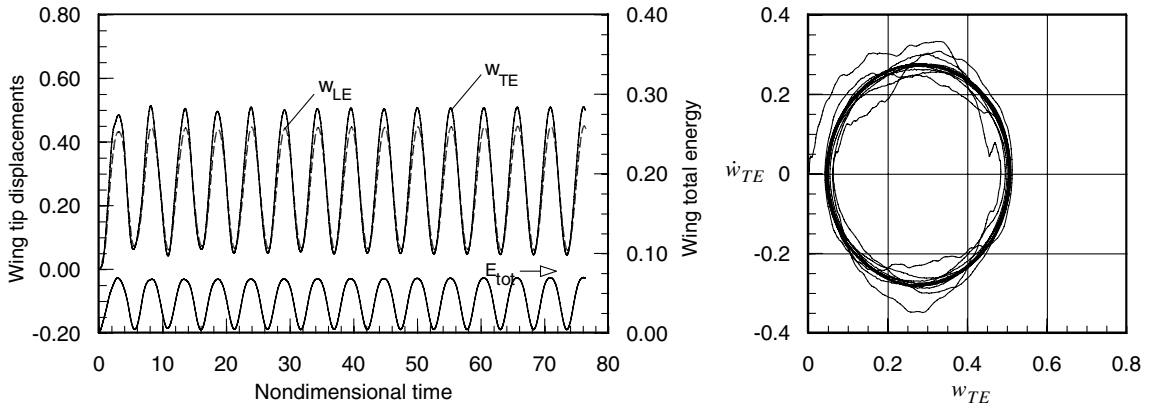

Fig. 8 Limit cycle flutter of the G-wing, as predicted by the fully nonlinear aeroelastic model (nonlinear structure and Euler-based aerodynamics) at Mach 0.865; $\rho_a = 0.4177\ \mathrm{kg/m^3}$; LCO frequency is 52.4 Hz.

essentially *nonconservative* nonlinear system, and classical concepts from nonlinear dynamics based on potential theory may not apply. At Mach 0.865, two stable limit cycles were observed, depending on the initial conditions (see Fig. 21b). It is likely that such nested LCOs extend to other neighboring Mach numbers as well.[§]

It should be noted that the temperature has been kept constant at the sea level, standard day value of 59°F (518.7°R) in these calculations. This would correspond to wind-tunnel tests during which the density and Mach number are varied while keeping the air temperature roughly constant at ambient conditions.

D. LCO Amplitude Versus Altitude

Because of strong interactions between the aeroelastic washout and the emerging flutter mode, limit cycle flutter can be observed over a wide range of altitudes (or air densities/dynamic pressures) in the present nonlinear time-marching flutter calculations. At Mach 0.865, for example, the LCO-type flutter of the G-wing persists down

[§]Additional calculations made after the paper was submitted indicate that the G-wing has nested LCOs throughout the transonic range [18].

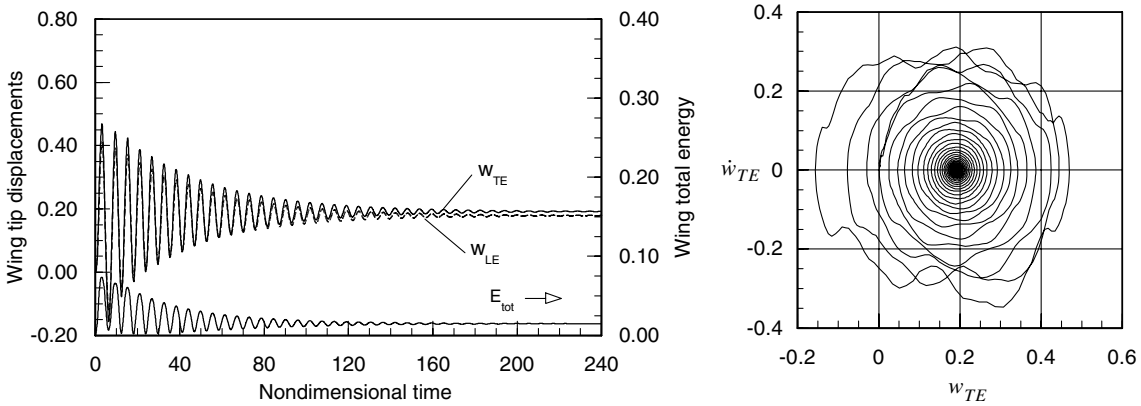

Fig. 9 Stable decay of the G-wing tip amplitudes at Mach 0.75; $\rho_a = 0.4177\ \mathrm{kg/m^3}$; aeroelastic mode frequency varies from 47.7 Hz (initial) to 47.2 Hz (final).

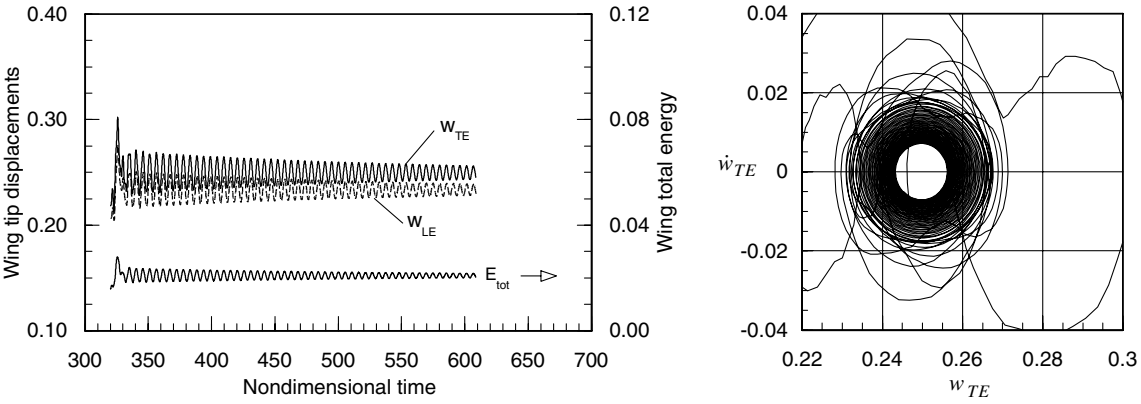

Fig. 10 Aeroelastic response of the G-wing at Mach 0.83, which is slightly below the flutter boundary; $\rho_a = 0.4177\ \mathrm{kg/m^3}$; aeroelastic mode frequency varies from 51.3 to 51.2 Hz.

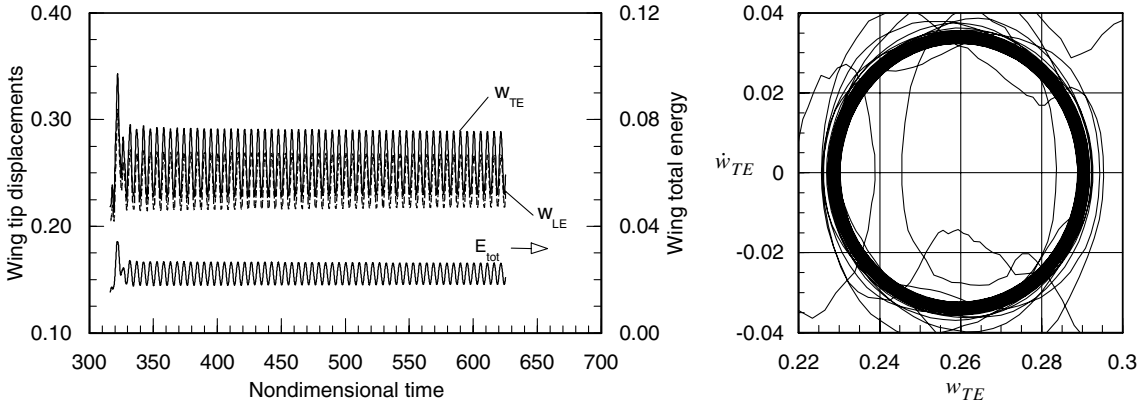

Fig. 11 Limit cycle flutter of the G-wing at Mach 0.84; $\rho_a = 0.4177\ \mathrm{kg/m^3}$; LCO frequency is about 51.7 Hz.

to very low densities, representing density altitudes well into the stratosphere (see Fig. 22). The behavior of the LCO amplitude with increasing altitude depends on Mach number as well, as shown in Fig. 23. Figure 23a shows the LCO amplitude versus altitude at Mach 0.865, which is roughly in the middle of the Mach number range in which stable LCOs are observed. In this case, the peak amplitude occurs around 33,000 ft (10 km) and shows a surprising reversal as the altitude is decreased toward sea level. As noted on the figure, this is a replot of Fig. 2 in terms of equivalent density altitude and does not include the effect of temperature. Figure 23b shows the corresponding plot at Mach 0.95, which is at the high end of the unstable LCO region, in which relatively strong amplitude growth occurs. Here, the flutter amplitude is seen to increase with altitude in the stratosphere and shows two local peaks in the troposphere, at around 24,000 and 30,000 ft. Furthermore, the wing is stable below about 15,000 ft. It should be noted that this plot includes the effect of temperature.

The reason for the local peaks in Fig. 23b is not known, but is suspected to be related to the properties of the atmosphere (i.e., the rate of temperature and density lapse versus altitude) and the relatively high sensitivity of the present nonlinear aeroelastic model of the G-wing to the aerodynamic loads. Temperature affects the flutter stability of the wing in two ways. At a given fixed Mach number, a decrease in air temperature (due to an increase in altitude in the troposphere, for example) lowers the air velocity relative to the wing, lowering the dynamic pressure for a given air density. Because

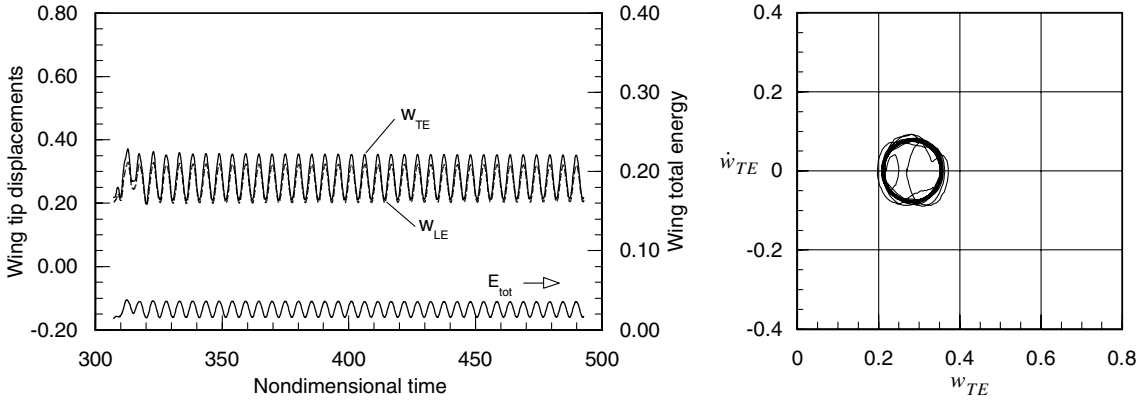

Fig. 12 Limit cycle flutter of the G-wing at Mach 0.865; $\rho_a = 0.4177$ kg/m^3; LCO frequency is about 52.2 Hz.

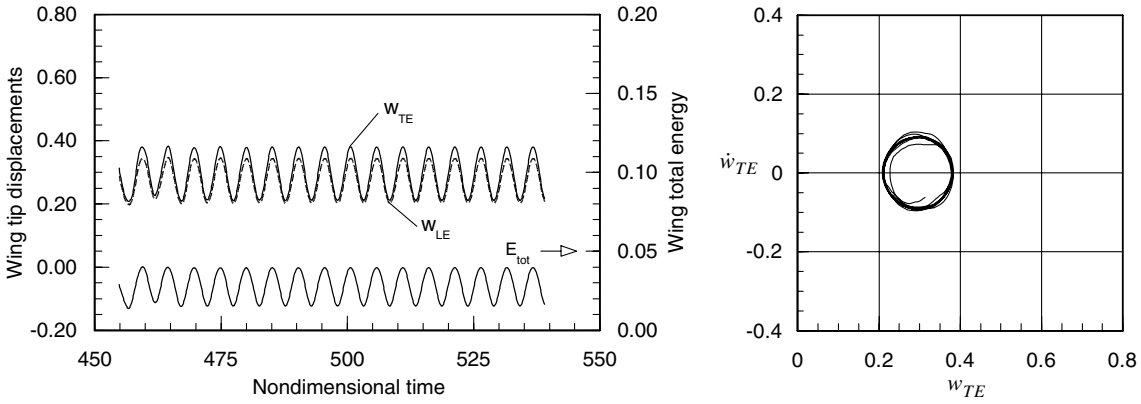

Fig. 13 Limit cycle flutter of the G-wing at Mach 0.88; $\rho_a = 0.4177$ kg/m^3; LCO frequency is 52.9 Hz.

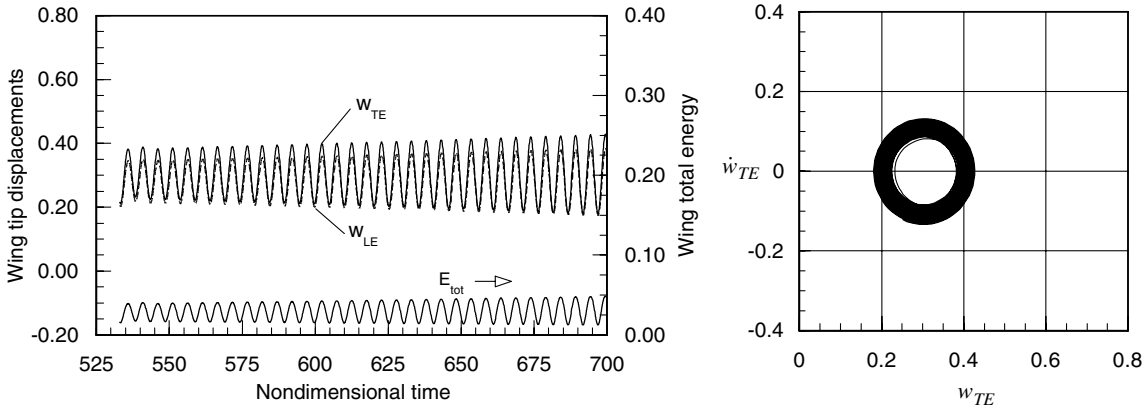

Fig. 14 Slowly growing limit cycle flutter of the G-wing at Mach 0.89; $\rho_a = 0.4177$ kg/m^3; LCO frequency is 53.3 Hz.

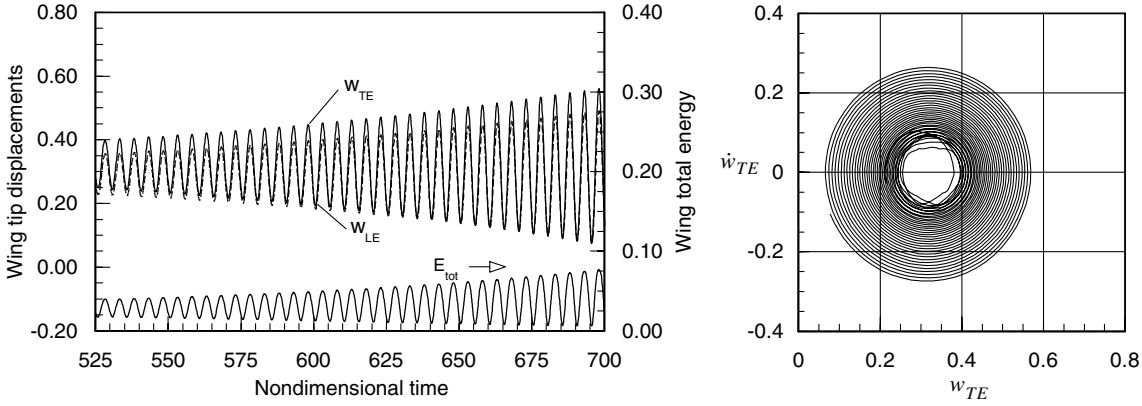

Fig. 15 Moderately growing flutter of the G-wing at Mach 0.92; $\rho_a = 0.4177$ kg/m^3; flutter frequency is 54.6 Hz.

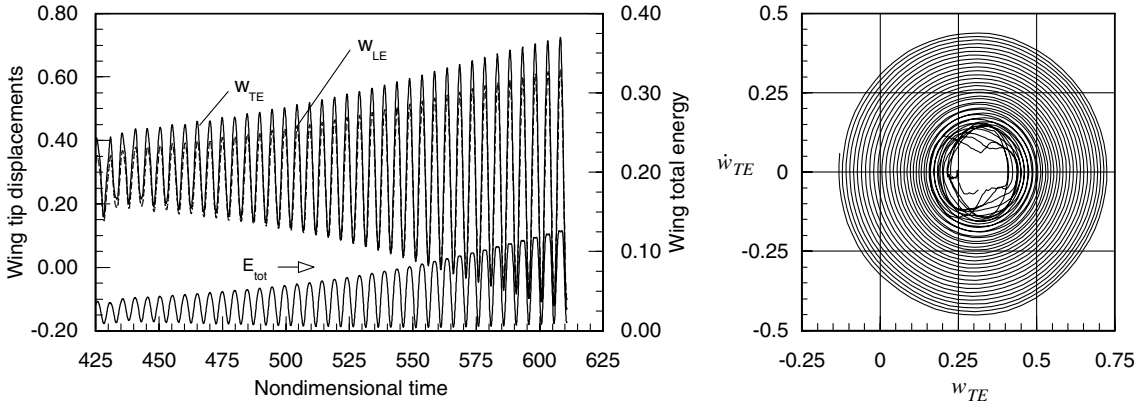

Fig. 16 Growing amplitude flutter of the G-wing at Mach 0.95; $\rho_a = 0.4177\ \mathrm{kg/m^3}$; flutter frequency varies from 57 Hz (initial) to 54.9 Hz (final).

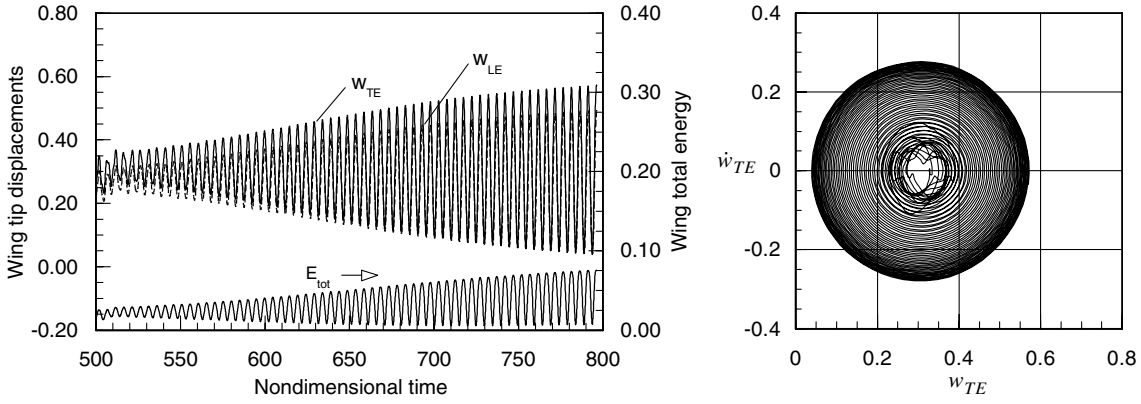

Fig. 17 Slow approach to high-amplitude limit cycle flutter of the G-wing at Mach 0.96; $\rho_a = 0.4177\ \mathrm{kg/m^3}$; LCO frequency is about 55.5 Hz (final).

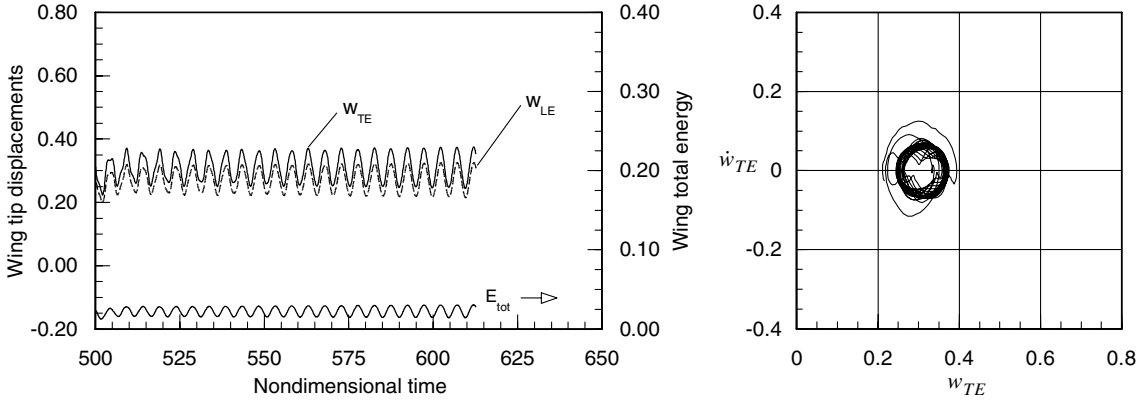

Fig. 18 Small-amplitude limit cycle flutter of the G-wing at Mach 0.965 ($\rho_a = 0.4177\ \mathrm{kg/m^3}$); two LCO frequencies are present: 60.7 and 51.2 Hz (initial); 56.7 and 54.8 Hz (final).

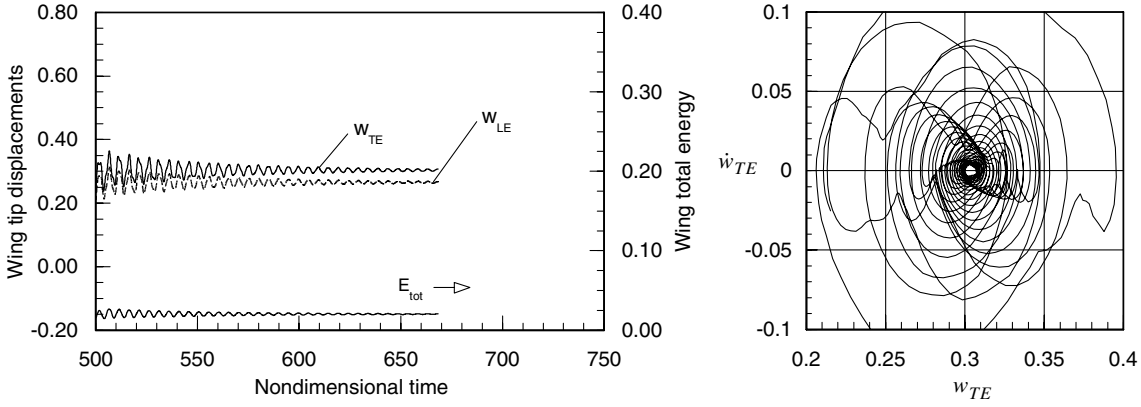

Fig. 19 Stable decay of the G-wing at Mach 0.97 ($\rho_a = 0.4177\ \mathrm{kg/m^3}$); two LCO frequencies at about 53 and 58.9 Hz are present at the end of the plot.

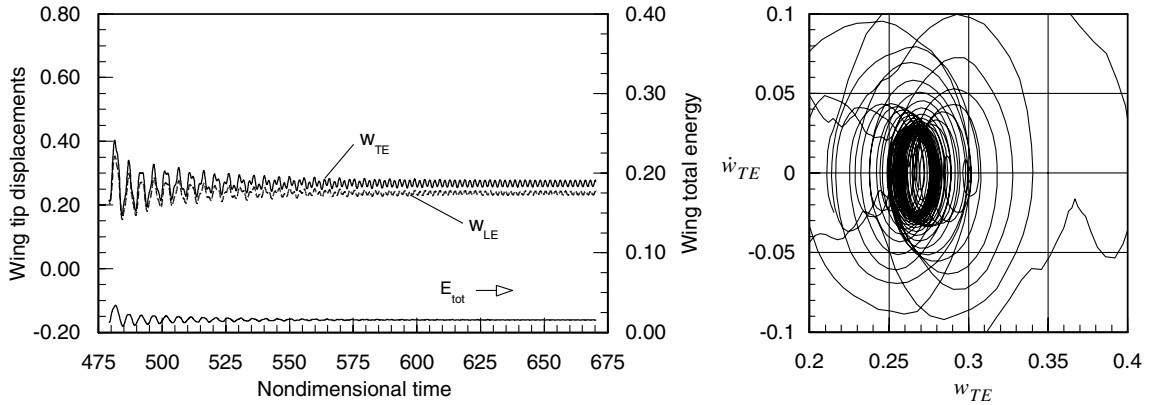

Fig. 20 Decay to a limit cycle of very small amplitude (G-wing at Mach 0.99; $\rho_a = 0.4177$ kg/m^3); final LCO frequency is about 138.4 Hz (and slightly decreasing).

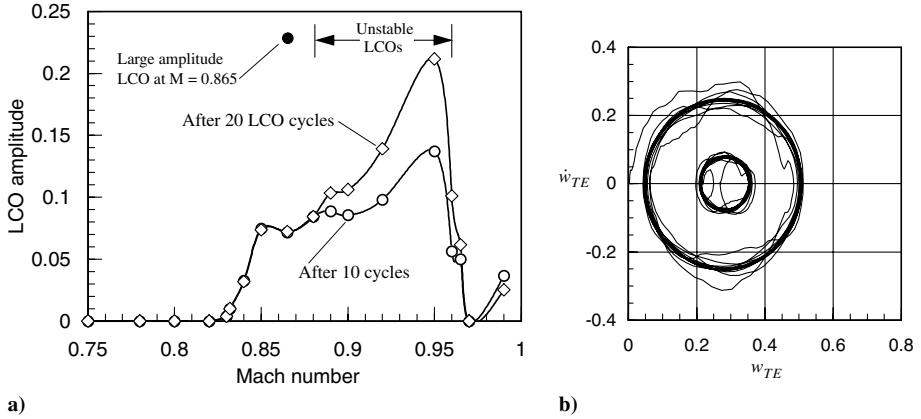

Fig. 21 Limit cycle flutter of a G-wing: a) limit cycle amplitude vs Mach number at a constant density $\rho_a = 0.4177$ kg/m^3, corresponding to a density altitude of approximately 32,800 ft (10,000 m) and b) nested LCOs of different amplitudes at Mach 0.865, depending on initial conditions; sea level, standard day temperature.

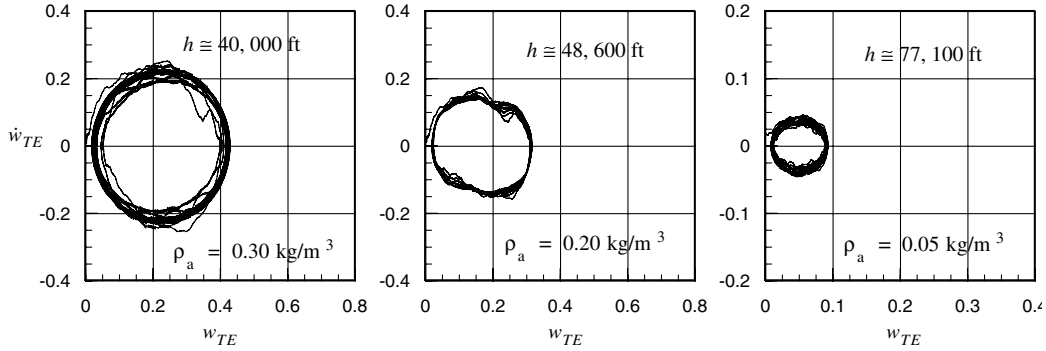

Fig. 22 Phase plots of LCO flutter at high altitudes ($M_\infty = 0.865$ and temperature effects neglected).

of the lower airspeed, the reduced velocity $U/b\omega_{1T}$ is also lowered. Both changes would be expected to have a stabilizing effect, based on linear flutter theories. But in the strongly nonlinear transonic range, we have demonstrated that a reduction in dynamic pressure at a fixed Mach number can in fact be destabilizing in some cases, because of the interactions between the aeroelastic washout and the shocks on the wing surface. The reduction in the reduced velocity, on the other hand, would still be expected to be stabilizing, although exceptions caused by nonlinear effects are possible in this case as well. Thus, all that can be said is that the effect of temperature must be determined on a case-by-case basis and would be expected to depend not only on the Mach number and altitude, but on the aeroelastic properties of the wing as well.

Our calculations indicate that it is primarily the aeroelastic washout effect that is responsible for the amplitude reversal reported in [9] and shown in Figs. 2 and 23a and for the failure of the linear structural code to predict the correct limit cycle flutter behavior. We also suspect that the structural washout is responsible for the persistence of LCO-type flutter of the G-wing over a wide range of air densities or altitudes. The in-plane degrees of freedom u and v of the wing (which are present in the nonlinear model only) appear to play a relatively minor destabilizing role in the LCO-type flutter of the G-wing.

The stabilizing role of the structural washout on transonic limit cycle flutter can be understood by examining the shock positions and shock dynamics during flutter. Figure 24 shows a comparison of the steady pressure coefficient at three outboard span locations on a rigid and a flexible wing, operating at Mach 0.865 and an angle of attack of 4.5 deg (wing root). The main effect of wing flexibility is to weaken the upper-surface shock and shift it forward, toward the leading edge,

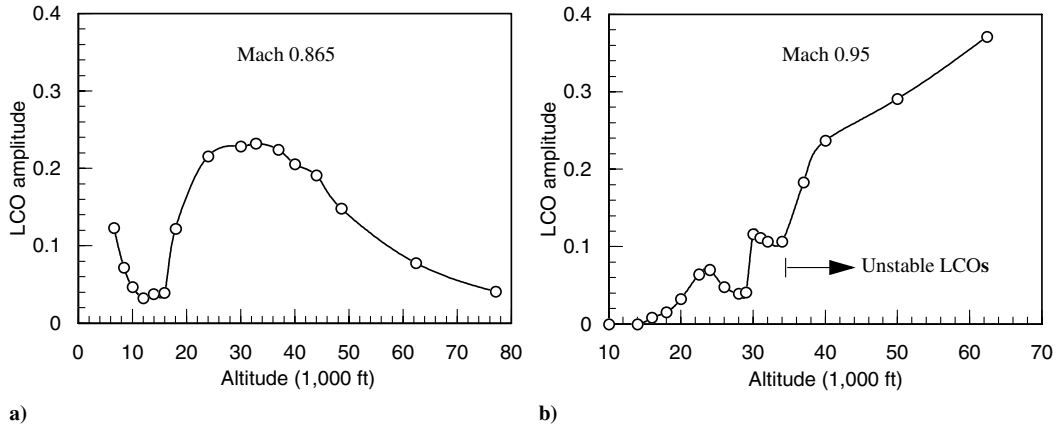

Fig. 23 Limit cycle flutter amplitude vs altitude at a constant Mach number: replot of Fig. 2 in terms of equivalent density altitude and a) does not include the effect of temperature (sea level, standard day temperature of 518.7°R is assumed) and b) includes the effect of temperature.

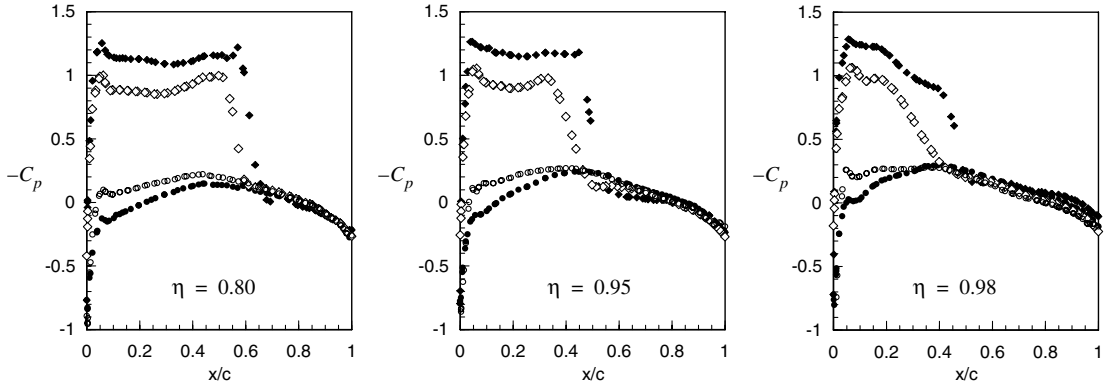

Fig. 24 Steady pressure distribution about the outboard region of the G-wing at Mach 0.865 and $\alpha = 4.5$ deg; $\rho_a = 0.4177$ kg/m^3; flexible wing (open symbols), rigid wing (solid symbols), upper surface (diamonds), and lower surface (circles).

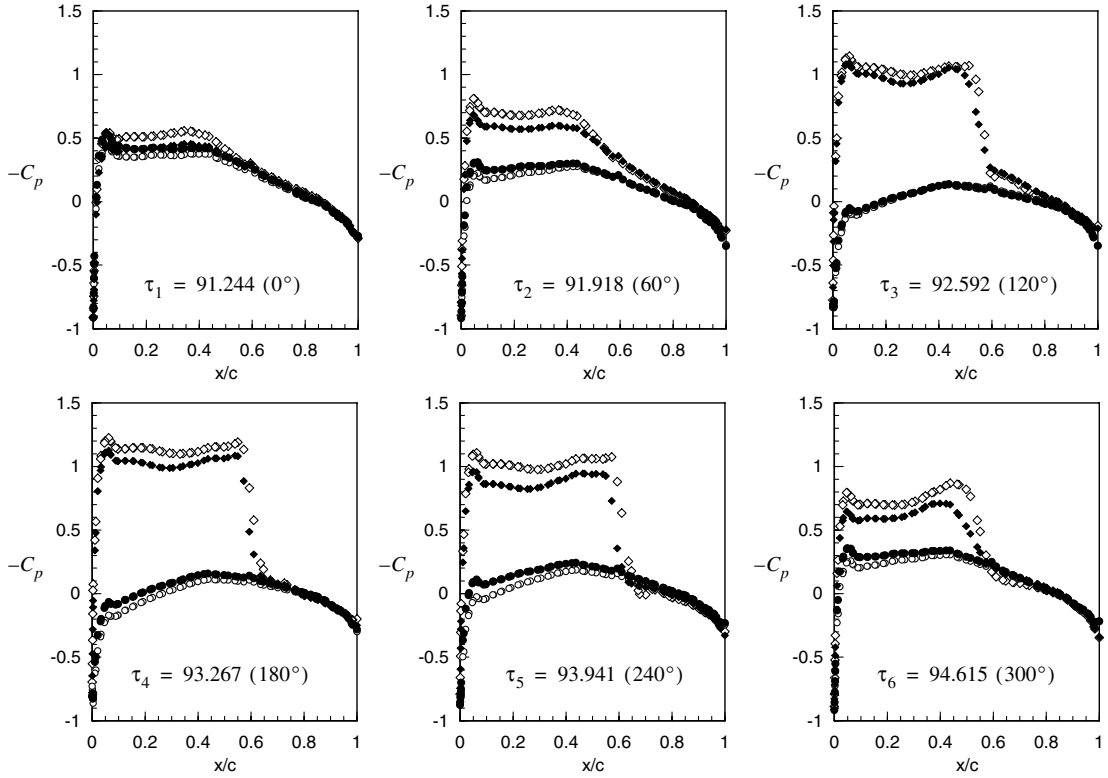

Fig. 25 Unsteady pressure distribution about the G-wing at 80% span location during LCO flutter at Mach 0.865 and $\alpha = 4.5$ deg; $\rho_a = 0.4177$ kg/m^3 (open symbols), $\rho_a = 0.75$ kg/m^3 (solid symbols) during second LCO flutter cycle after abrupt air density change from $\rho_a = 0.4177$ to 0.75 kg/m^3, upper surface (diamonds), and lower surface (circles).

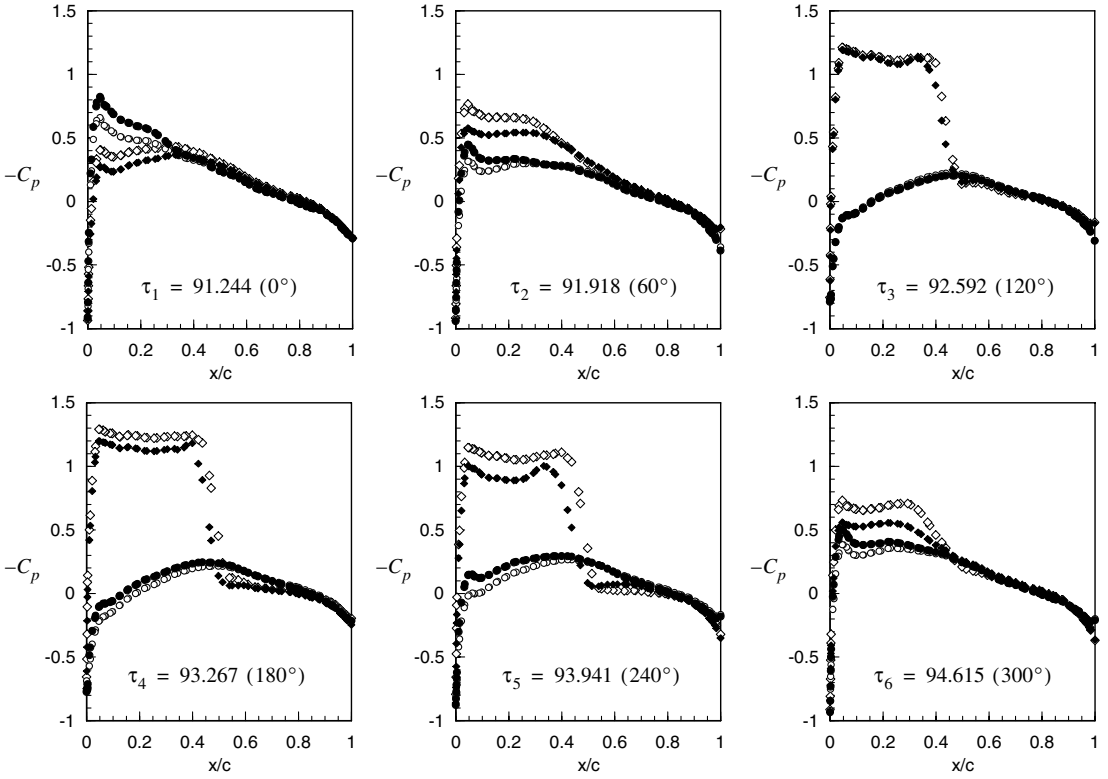

Fig. 26 Unsteady pressure distribution about the G-wing at 95% span location during LCO flutter at Mach 0.865 and $\alpha = 4.5$ deg; $\rho_a = 0.4177$ kg/m^3 (open symbols), $\rho_a = 0.75$ kg/m^3 (solid symbols) during second LCO flutter cycle after abrupt air density change from $\rho_a = 0.4177$ to 0.75 kg/m^3, upper surface (diamonds), and lower surface (circles).

which is stabilizing from a flutter standpoint. At the same time, the peak Mach numbers (not shown) in the supersonic regions are reduced at all span locations, which is also expected to be stabilizing for most transonic Mach numbers, as it is qualitatively similar to the effect of reducing the flight or freestream Mach number.[¶] The structural washout results in a reduction of the aerodynamic loading as the wing untwists, brought about by a reduction of the streamwise angle of attack as the wing bends in the positive (upward) direction (Fig. 1). This aeroelastic unloading is accompanied by a reduction in the Mach numbers in the supersonic region, which is qualitatively similar to a reduction of the effective freestream Mach number.

From these observations, one would expect that the structural washout effect should lead to an earlier transition from Tijdeman type A (continuous) to type B (intermittent) shock motion and this transition should occur at a lower LCO amplitude. Earlier studies [5,19] have shown that the A-to-B transition in the shock motion dynamics is strongly stabilizing, as it limits the ability of the wing to extract energy from the airstream, typically turning an exponentially growing flutter mode into LCO-type flutter. In the case of the G-wing at Mach 0.865, for example, the outer limit cycle shown in Figs. 8 and 21b is associated with intermittent shock motion on the upper surface of the wing, as is evident from Fig. 25. Figure 25 shows the instantaneous (unsteady) pressure distribution on the upper and lower wing surfaces at the 80% span location during LCO flutter at Mach 0.865 at two different air densities: $\rho_a = 0.4177$ and 0.75 kg/m^3, corresponding to density altitudes of roughly 10 km (32,800 ft) and 4.85 km (15,900 ft), respectively. As these densities correspond to extreme points on the LCO amplitude vs density plot in Fig. 2, additional flutter simulations were run to obtain instantaneous pressure and Mach number distributions for the purpose of identifying the differences in shock positions and strengths and shock dynamics during flutter in an attempt to identify the mechanism behind the amplitude reversal with increasing air density.

[¶]An exception may occur slightly past the transonic dip, where a decrease in Mach number may be destabilizing.

In one such calculation, the stable outer LCO at Mach 0.865 and $\rho_a = 0.4177$ kg/m^3 was first established, then the air density was abruptly increased to 0.75 kg/m^3 and the time-marching calculations continued. Snapshots of instantaneous unsteady pressure and Mach number distributions about the wing at 20 different span stations were calculated. Representative results for the outboard region of the wing are shown in Figs. 25–27. Figure 25 shows the unsteady pressure coefficients at 80% span for the 0.75 kg/m^3 case at 6 different times during the second LCO cycle after the abrupt density increase, as well as the corresponding pressure coefficients during the last LCO cycle for the $\rho_a =$ 0.4177 kg/m^3 case. The nondimensional times shown correspond to the 0.75 kg/m^3 case, starting at the point of maximum wing tip deflection and spaced 60 deg apart in temporal phase. It should be noted that the differences in aeroelastic frequencies for the two cases have been accounted for in the comparisons, to make each snapshot represent the same temporal phase within the corresponding aeroelastic cycle. In each case, intermittent (type B) shock motion is observed. Figure 26 shows the corresponding comparisons at the 95% span location. Figure 27 shows the aeroelastic response of the wing tip and the decay of the wing energy $E_{\text{tot}} = T + U$ vs time. It is apparent from these figures that the unsteady flow and the aeroelastic response of the wing adjust rather rapidly to the abrupt change in air density, and there is already a noticeable shift forward and a weakening of the upper-surface shocks during the second aeroelastic cycle after the density change. From Fig. 27 it is evident that this shift and accompanying weakening of the shocks are strongly stabilizing, and the wing oscillations in this case do not converge to the inner small-amplitude LCO indicated in Fig. 2, but instead decay to zero. This undershoot is believed to be caused by aeroelastic inertia and the possibility that the lower LCO may be unstable or, at best, semistable [18].

Figure 28 shows the instantaneous pressure distributions at 95% span during the 59th cycle after the step change in air density. By now, significant weakening of the upper-surface shock has taken place and the shock motion has become continuous. The aeroelastic amplitudes have decayed to only a few percent of the initial LCO amplitudes (see Fig. 27).

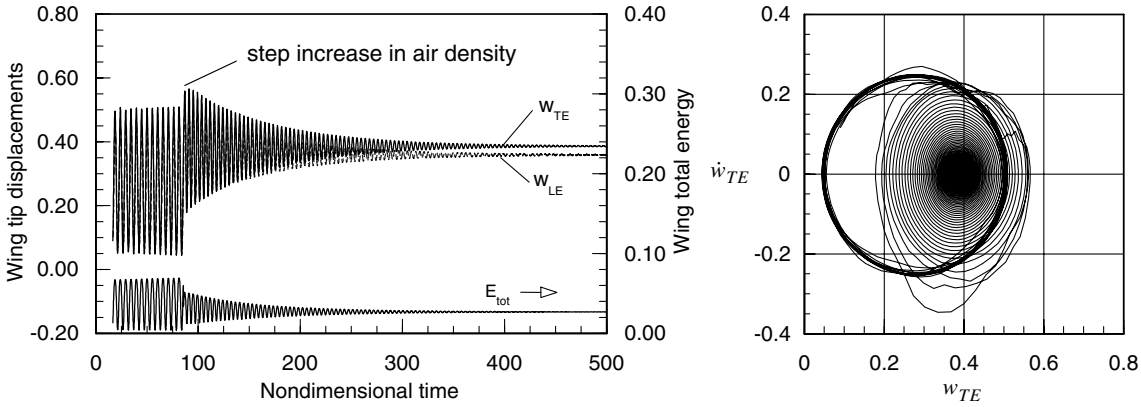

Fig. 27 Quenching of limit cycle flutter of G-wing at Mach 0.865 by increasing the air density from $\rho_a = 0.4177$ to 0.75 kg/m^3, corresponding to a decrease in density altitude from 32,800 to 15,900 ft.

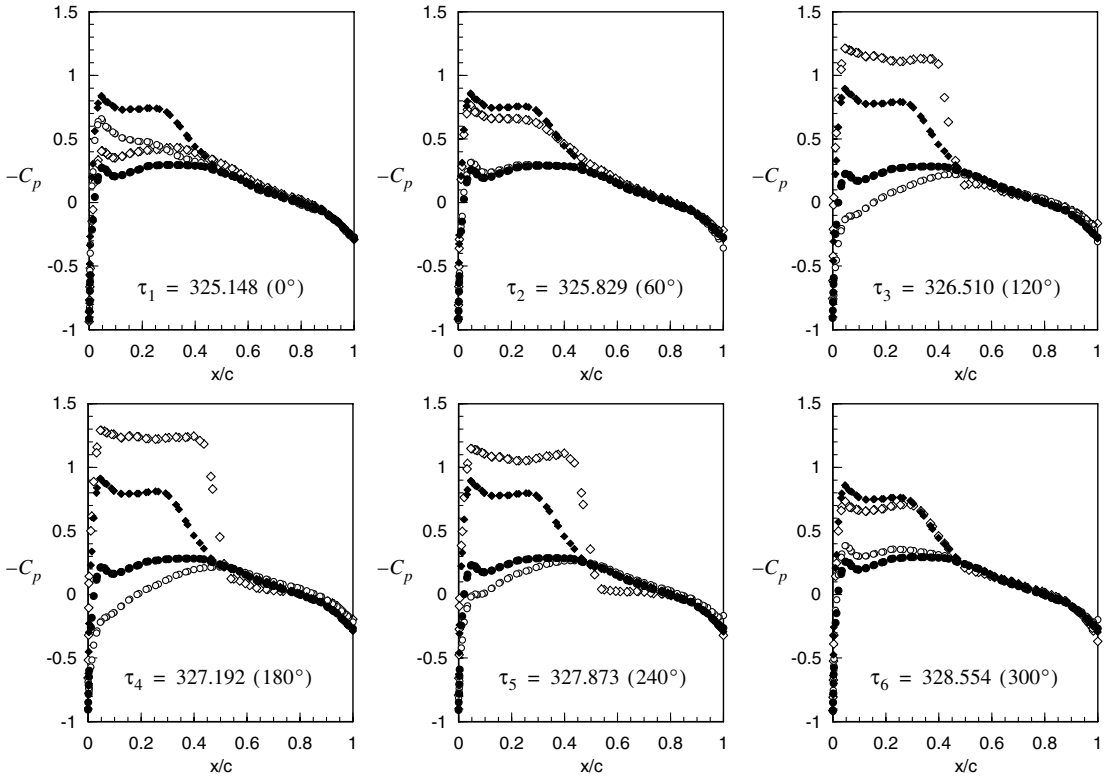

Fig. 28 Unsteady pressure distribution about the G-wing at 95% span location during LCO flutter at Mach 0.865 and $\alpha = 4.5$ deg; $\rho_a = 0.4177$ kg/m^3 (open symbols), $\rho_a = 0.75$ kg/m^3 (solid symbols) during 59th LCO flutter cycle after abrupt air density change from $\rho_a = 0.4177$ to 0.75 kg/m^3, upper surface (diamonds), and lower surface (circles).

IV. Conclusions

1) The aeroelastic mechanism responsible for the observed limit cycle flutter of the Göttingen wing and the G-wing studied in this paper appears to be closely linked to the structural washout effect.

2) As the wing bending amplitude increases, the aeroelastic washout reduces the angle of attack of streamwise chord sections, unloading the outboard region and reducing the shock strength. The weaker and more forward shocks lead to an earlier transition from type A to type B shock motion, at relatively small flutter amplitudes, limiting the ability of the wing to extract energy from the airstream.

3) The large discrepancy between the LCO flutter behaviors predicted using the linear-vs-nonlinear structural models can be understood by considering the stabilizing effect of washout. Although the nonlinear structure is stiffer than the linear structure, it is actually less stable because the structural washout is also less.

4) The LCO amplitude reversal vs air density arises because of strong interactions between the structural and aerodynamic nonlinearities, through the aeroelastic washout mechanism.

5) At Mach 0.865, the LCO amplitudes of the G-wing peak at around a density altitude of 33,000 ft. If sufficient structural damping is added, the wing will be flutter-free at the lower altitudes, but not at higher altitudes. At higher transonic Mach numbers, at or close to Mach 0.95, the flutter amplitudes continue to grow with altitude well into the stratosphere, but the wing is stable below about 15,000 ft.

6) The LCO-type flutter of the G-wing is a *transonic* phenomenon. No limit cycle flutter was observed at subcritical Mach numbers. Flutter onset is slightly below Mach 0.84, and the LCO amplitudes grow until Mach 0.95 is reached, at which point they start decreasing, vanishing abruptly around Mach 0.97.

7) At Mach 0.865, there are indications that multiple (nested) LCOs may be present, and the limit cycle amplitude depends on the initial conditions.

Acknowledgments

This research was supported by NASA grant NCC 4-157 and NASA contract NND05AD23P.

References

[1] Denegri, C. M., "Limit Cycle Oscillation Flight Test Results of a Fighter Wing with External Stores," *Journal of Aircraft*, Vol. 37, No. 5, Sept.–Oct. 2000, pp. 761–769. doi:10.2514/2.2696

[2] Edwards, J. W., Schuster, D. M., Keller, D. F., and Moses, R. W., "MAVRIC Flutter Model Transonic Limit Cycle Oscillation Test," NASA TM-2001-210877, May 2001.

[3] Cunningham, A. M., Jr., "Buzz, Buffet, and LCO on Military Aircraft: The Aeroelastician's Nightmare," *Proceedings of the International Forum on Structural Dynamics and Aeroelasticity 2003* [CD-ROM], Netherlands Association of Aeronautical Engineers, Amsterdam, 4–6 June 2003.

[4] Attar, P. J., Dowell, E. H., and White, J. R., "Modeling Delta Wing Limit-Cycle Oscillations Using a High-Fidelity Structural Model," *Journal of Aircraft*, Vol. 42, No. 5., Sept.–Oct. 2005, pp. 1209–1217. doi:10.2514/1.11325

[5] Bendiksen, O. O., "Transonic Limit Cycle Flutter/LCO," AIAA/ASME/ASCE/AHS/ASC 45th Structures, Structural Dynamics, and Materials Conference, AIAA Paper 2004-1694, Palm Springs, CA, Apr. 2004.

[6] Schewe, G., Knipfer, A., Mai, H., and Dietz, G., "Experimental and Numerical Investigation of Nonlinear Effects in Transonic Flutter," DLR, German Aerospace Center, Paper DLR IB 232-2002 J01, 2002.

[7] Schewe, G., Mai, H., and Dietz, G., "Nonlinear Effects in Transonic Flutter withe Emphasis on Manifestations of Limit Cycle Oscillations," *Journal of Fluids and Structures*, Vol. 18, No. 1, 2003, pp. 3–22. doi:10.1016/S0889-9746(03)00085-9

[8] Dietz, G., Schewe, G., Kiessling, F., and Sinapius, M., "Limit-Cycle-Oscillation Experiments at a Transport Aircraft Wing Model," *Proceedings of the International Forum on Structural Dynamics and Aeroelasticity 2003* [CD-ROM], Netherlands Association of Aeronautical Engineers, Amsterdam, 4–6 June 2003.

[9] Bendiksen, O. O., "Transonic Limit Cycle Flutter of High-Aspect-Ratio Swept Wings," *Journal of Aircraft*, Vol. 45, No. 5, Sept.–Oct. 2008, pp. 1522–1533; also AIAA Paper 2006-1635, May 2006. doi:10.2514/1.29547

[10] Seber, G., and Bendiksen, O. O., "Nonlinear Flutter Calculations Using Finite Elements in a Direct Eulerian–Lagrangian Formulation," *AIAA Journal*, Vol. 46, No. 6, June 2008, pp. 1331–1341; also AIAA Paper 2005-1856, Apr. 2005. doi:10.2514/1.27844

[11] Batoz, J. L., and Lardeur, P., "A Discrete Shear Triangular Nine D.O.F. Element for Analysis of Thick to Very Thin Plates," *International Journal for Numerical Methods in Engineering*, Vol. 28, No. 3, 1989, pp. 533–560. doi:10.1002/nme.1620280305

[12] Bendiksen, O. O., "Modern Developments in Computational Aeroelasticity," *Proceedings of the Institution of Mechanical Engineers, Part G (Journal of Aerospace Engineering)*, Vol. 218, No. 3, June 2004, pp. 157–178. doi:10.1243/0954410041872861

[13] Jameson, A., and Mavriplis, D. J., "Finite Volume Solution of the Two-Dimensional Euler Equations on a Regular Triangular Mesh," AIAA Paper 85-0435, Jan. 1985.

[14] Mavriplis, D. J., "Accurate Multigrid Solution of the Euler Equations on Unstructured and Adaptive Meshes," *AIAA Journal*, Vol. 28., Feb. 1990, pp. 213–221. doi:10.2514/3.10377

[15] Davis, G. A., and Bendiksen, O. O., "Unsteady Transonic Two-Dimensional Euler Solutions Using Finite Elements," *AIAA Journal*, Vol. 31, June 1993, pp. 1051–1059. doi:10.2514/3.11728

[16] Hwang, G., "Parallel Finite Element Solutions of Nonlinear Aeroelastic and Aeroservoelastic Problems in Three-Dimensional Transonic Flows," Ph.D. Dissertation, Mechanical and Aerospace Engineering Dept., Univ. of California, Los Angeles, CA, Mar. 1997.

[17] Bohr, H., *Almost Periodic Functions*, Chelsea, New York, 1947.

[18] Bendiksen, O. O., "Multiple Limit Cycles in Transonic Flow and Some Computational and Experimental Implications," *AVT-152 Symposium on Limit Cycle Oscillation and Other Amplitude-Limited Self Excited Oscillations*, NATO Paper AVT-152-024, May 2008.

[19] Bendiksen, O. O., "Role of Shocks Dynamics in Transonic Flutter," *Proceedings of the AIAA Dynamics Specialists Conference*, AIAA, Reston, VA, Apr. 1992, pp. 401–414; also AIAA Paper 92-2121.